Available online at www.sciencedirect.com
ScienceDirect
Journal of Sound and Vibration 311 (2008) 1100–1113
JOURNAL OF SOUND AND VIBRATION
www.elsevier.com/locate/jsvi

A combined time and frequency domain approach for acoustic resonance prediction

J.C. Chassaing[a,*], A.I. Sayma[b], M. Imregun[b]

[a]*Université Pierre et Marie Curie, Institut Jean Le Rond d'Alembert, case 161, 4 place Jussieu, 75252 Paris, France*
[b]*Imperial College London, Department of Mechanical Engineering, South Kensington Campus, London SW7 2AZ, UK*

Received 22 March 2007; received in revised form 25 September 2007; accepted 2 October 2007
Available online 7 November 2007

Abstract

A general hybrid time- and frequency-domain methodology has been developed to identify acoustic resonance conditions of internal flow configurations. The acoustic modes are determined by imposing onto the flow a time-dependent excitation at several locations on the boundary. The resulting time-domain pressure responses, which are computed via an unsteady Favre–Reynolds averaged Navier–Stokes solver, are used to determine the frequency response function matrix of the fluid which can be considered to be a multiple-input multiple-output system. The main test case was selected to be a closed-end cylindrical duct for which the effect of different excitation techniques on the predicted acoustic modes is discussed in detail. The last test case deals with the acoustic characterization of a 2-D channel with symmetric bumps and an inlet flow velocity of $17\,m\,s^{-1}$. It is shown that the methodology was suitable for identifying axial and transverse acoustic modes up to 3 kHz.

1. Introduction

In many aerospace applications, aeroacoustic resonances of internal flow configurations are considered to be extremely undesirable phenomena which must be avoided during the design process. The excitation of the acoustic modes in core volumes, such as the combustion chamber of liquid-propellant [1,2] or solid-propellant [3–5] rocket motors, can lead to uncontrolled self-sustained instabilities. Similarly, under critical conditions, rotors of high-pressure turbo-compressors can exhibit high vibration levels due to wake-excited acoustic resonances [6]. Acoustic/flow coupling can also play a crucial role on performance degradations and extra tone noise levels of configurations such as shock wave/boundary layer interactions [7], convergent-divergent nozzles at off-design conditions [8] and open-cavities flow resonance [9].

Analytical methods are limited to simple cases and the use of numerical methods for acoustic resonance predictions of complex geometries with flow-acoustic coupling is not straightforward. Such difficulties were addressed by Eriksson et al. [10] for the prediction of the afterburner rumble and screech. Their approach is based on an Arnoldi procedure to extract the acoustic eigenmodes from the linearized Euler equations solved

*Corresponding author. Tel.: +33 144 2788 14; fax: +33 144 2788 78.
E-mail addresses: jean-camille.chassaing@upmc.fr (J.C. Chassaing), a.sayma@imperial.ac.uk (A.I. Sayma), m.imregun@imperial.ac.uk (M. Imregun).

0022-460X/$ - see front matter © 2007 Elsevier Ltd. All rights reserved.
doi:10.1016/j.jsv.2007.10.006

Nomenclature

a	sound velocity
c	viscous damping
$E[.]$	expectation operator
f_{ex}	excitation frequency
f_n	undamped natural frequency
G_{xx}	one-sided auto-spectrum density function ($\in \mathbb{C}^{N_i \times N_i}$)
G_{xy}	one-sided cross-spectrum density function ($\in \mathbb{C}^{N_i \times N_o}$)
H_{xy}	frequency-response function ($\in \mathbb{C}^{N_i \times N_o}$)
k	stiffness
L	length
m	mass
n	mode number
n_{max}	number of time steps
N_i	number of inputs
N_k	number of samples
N_o	number of outputs
R	radius
S_{xy}	cross-spectrum density function ($\in \mathbb{C}^{N_i \times N_o}$)
t	time
t_{max}	total simulation time
$x(t)$	input signal
$y(t)$	output signal
$X(f)$	forward Fourier transform of the input
$Y(f)$	forward Fourier transform of the output
Δf	frequency resolution
$\phi(f)$	phase factor of $H_{xy}(f)$
∂S	surface of the vibrating wall

Subscripts

i	input
i,j,k	vector component along the corresponding direction
k	sample number
n	mode number
o	output

Superscripts

nA	nth axial mode number
T	transpose
$*$	complex conjugate

in the time-domain. An alternative experimental approach to establish possible links between observed instabilities and acoustic resonances is based on white-noise excitation of the component under study and the filtering of acoustic resonance frequencies by using loudspeakers [11,12,14–16]. In many cases, such simple acoustic characterization may well provide crucial information about flow-induced resonant sound generation during operating conditions [17,18]. Due to significant improvements in computational fluid dynamics methods, turbulence modeling and computing hardware, unsteady Reynolds-averaged Navier–Stokes (RANS) equations can, in principle, be used for time-domain investigations of acoustic resonance phenomena [19–21]. However, neither the application of a suitable excitation to identify the acoustic resonances without altering the nature of the flow, nor the interpretation of the results is straightforward.

This paper aims at developing a general time-domain RANS-based methodology to identify acoustic resonances of core volumes commonly encountered in aeronautical applications. The novelty of the approach, which can be integrated in the design process of engineering geometries, is the representation of the flow domain by means of generalized transfer functions from which the acoustic resonances are deduced. Such transfer functions are computed from the response of the flow to small perturbations that are imposed onto the flow at several locations at the boundaries using a standard CFD code. The formulation is totally general and can be used with any geometry subjected to any flow. The difficulties associated with imposing an optimum perturbation not to disturb the main flow while obtaining an adequate response and the selection of other numerical parameters are discussed in detail.

2. Basic methodology

The dynamic behavior of a multiple-input multiple-output (MIMO) linear system can be described through the following frequency-domain relationship

$$\mathbf{H}_{xy}(f) = \mathbf{G}_{xx}^{-1}(f)\mathbf{G}_{xy}(f), \tag{1}$$

where $\mathbf{H}_{xy} \in \mathbb{C}^{N_i \times N_o}$ is the complex-valued matrix of frequency-response functions (FRF matrix) between the N_i inputs and the N_o outputs of the system, $\mathbf{G}_{xx} \in \mathbb{R}^{N_i \times N_i}$ is the real-valued squared matrix of the $N_i \times N_i$ one-sided auto-spectral density of the inputs, and $\mathbf{G}_{xy} \in \mathbb{C}^{N_i \times N_o}$ is the complex-valued rectangular matrix of the $N_i \times N_o$ cross-spectral density between the N_i inputs and the N_o outputs. The auto- and cross-spectral density matrices are determined by

$$\mathbf{G}_{xx}(f) = 2 \lim_{T \to \infty} \frac{1}{T} E[\mathbf{X}^*(f)\mathbf{X}^{\mathrm{T}}(f)], \tag{2}$$

$$\mathbf{G}_{xy}(f) = 2 \lim_{T \to \infty} \frac{1}{T} E[\mathbf{X}^*(f)\mathbf{Y}^{\mathrm{T}}(f)], \tag{3}$$

where E denotes the expectation operator and $\mathbf{X} = [X_1, X_2, \ldots, X_{N_i}]^{\mathrm{T}}$ and $\mathbf{Y} = [Y_1, Y_2, \ldots, Y_{N_o}]^{\mathrm{T}}$ are two vectors representing the Fourier transform of the N_i inputs and the N_o outputs, respectively. The inverse of the auto-correlation matrix $\mathbf{G}_{xx}^{-1}$ is computed using singular value decomposition. From a practical point of view, the record time is finite since the numerical simulation with the RANS code is for a finite duration. Consequently, Eq. (1) gives only an approximation to the FRF matrix.

In the present work, the inputs correspond to time-dependent excitations which are applied at several boundary locations to the flow. The response is computed at several locations inside the core volume solving the Favre–Reynolds-averaged Navier–Stokes equations. Such time-domain information allows the construction of a frequency response function of the core volume from which both the acoustic resonances and associated mode shapes are determined. Because the resonance frequency range investigated in this study is below 3 kHz, it is assumed that the time-scales of interest are correctly resolved with the RANS approach.

3. Test-case 1: 1-dof mechanical system

The previous methodology is validated by comparison with the exact transfer function of a single-input single-output configuration. A viscously damped 1-dof mechanical system is excited by a stationary random forcing function and the corresponding time-domain equation of motion are

$$m\ddot{y}(t) + c\dot{y}(t) + ky(t) = x(t), \tag{4}$$

where $m = 17.5\,\mathrm{kg}$ is the mass of the system, $c = 350\,\mathrm{N\,s\,m^{-1}}$ denotes the viscous damping coefficient, $k = 1.7 \times 10^4\,\mathrm{kN\,m^{-1}}$ is the stiffness coefficient, $x(t)$ and $y(t)$ are, respectively, the input random force and the resulting output displacement. A 4-step Runge–Kutta finite difference scheme is used to compute the time-domain response of the system used to identify the frequency-response function. The random behavior of the input force $x(t)$ is prescribed within a range of $\pm 4.5\,\mathrm{N}$ and a different value of the input signal is imposed at each time step $\Delta t = 10^{-4}\,\mathrm{s}$. Results are compared with the exact solution of the frequency-response function [22, pp. 33–40].

$$|H_{xy}(f)| = \{k\sqrt{[1 - (f/f_n)^2]^2 + [2\xi f/f_n]^2}\}^{-1}, \tag{5}$$

where $\xi = c/(2\sqrt{km})$ denotes the damping factor and $f_n = 1/(2\pi)\sqrt{(k/m)}$ represents the undamped natural frequency.

A comparison of the gain factor between the analytical solution and two numerical results is given in Fig. 1. The first numerical result is obtained using only one sample record ($N_k = 1$) and the frequency-response function is determined from the auto- and cross-spectrum one-sided density functions G_{xx} and G_{xy} (Eqs. (2) and (3)). The Fourier transforms of the input and output signal are computed over a single record time of length $T = 0.2047\,\mathrm{s}$ corresponding to $n_{\max} = 2048$ iterations. This procedure is sufficient to give a good estimation of the resonance frequency as shown by the position of the peak in the gain factor distribution (Fig. 1) where the exact solution and the computed resonance frequencies are $f_r^{\mathrm{exact}} = 158.34\,\mathrm{Hz}$ and $f_r^{\mathrm{comp.}} = 162.9\,\mathrm{Hz}$, respectively, for a frequency resolution of $\Delta f = 4.88\,\mathrm{Hz}$. However, these predictions become unacceptable for very high frequencies, introducing substantial spurious noise. A second computational test was performed defining the total computational time $T_{\max} = N_k T$ based on a multiple of the previous record length T, and on the total number of the sample records N_k.

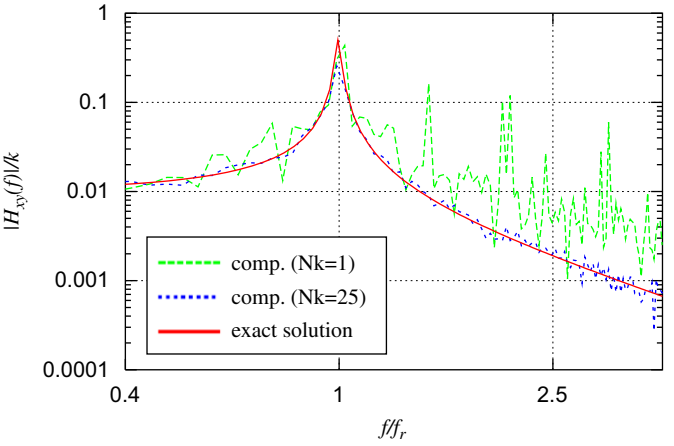

Fig. 1. Comparison of exact and computed frequency response functions for the 1-dof mechanical system.

In the case of the results presented in Fig. 1, the number of sample records is $N_k = 25$ and the length of each sample record remains unchanged ($T = 0.2047$ s and $n_{\max} = 2048$). The main effect of averaging over several sample signals when computing the frequency-response function results in a substantial smoothing of the numerical solution. It can be observed that the computed value of the resonance frequency with $N_k = 25$ ($f_r = 157.4$ Hz) is closer to the exact solution of $f_r^{\text{exact}} = 158.34$ Hz as compared with $f_r = 162.9$ Hz for $N_k = 1$. Furthermore, the shape of the gain factor distribution is corrected when the frequency increases, giving a mean slope after the peak which can be superimposed to the slope of the exact solution. Similar improvements were obtained on the phase factor prediction where the phase shift near the resonance frequency was in satisfactory agreement with the exact solution.

4. Test-case 2: acoustic resonance in a closed-end tube

The purpose of the second test case is to validate the present methodology for the zero-flow acoustic characterization of a closed-end tube. This configuration was used by Anthoine et al. [11] for comparison with the measurements of acoustic resonance frequencies in a typical solid propellant booster [11–14]. This axisymmetric test facility consists of a contoured nozzle with a throat diameter of 30 mm, a section diameter of 76 mm and a booster length ($L = 405$ mm). In order to get a better understanding of the flow-acoustic coupling mechanisms in such configuration, Anthoine et al. [11] began their experimental investigations by a preliminary study where a loudspeaker is placed at the throat of the nozzle whereas the original porous wall at the right end is replaced by a solid wall so that the duct has closed ends. The experimentally determined frequencies of the first two axial acoustical modes were found to be relatively close to the analytically determined resonance frequencies of a circular cylinder with close-ends. Consequently, here it will be assumed, that the acoustic characterization of booster could be approximated by a cylinder of diameter 76 mm without any loss of generality [11,13]. An unstructured mesh was generated using 31 circumferential nodes, each duct end surface was discretized with triangular elements and 56 nodes were used along the length of the cylinder with quadrilateral elements (Fig. 2).

The main difficulty is the formulation of a suitable unsteady excitation mechanism similar to white-noise that would be provided by a loudspeaker. After many attempts, it was found that best results were obtained when the left end surface of the duct was modeled with an elastic membrane subject to random deformations of the form:

$$x_{i,j,k}(t) = x^0_{i,j,k} + \chi_{i,j,k}(t)\cos[2\pi f_{\text{ex}}(t)t] \quad \forall (i,j,k) \ \in \partial S, \tag{6}$$

where ∂S denotes the surface of the vibrating wall, $x_{i,j,k}$ is the instantaneous position of the wall at node (i,j,k), $x^0_{i,j,k}$ determines the unperturbed position of the membrane, $\chi_{i,j,k}$ is the maximum vibration amplitude

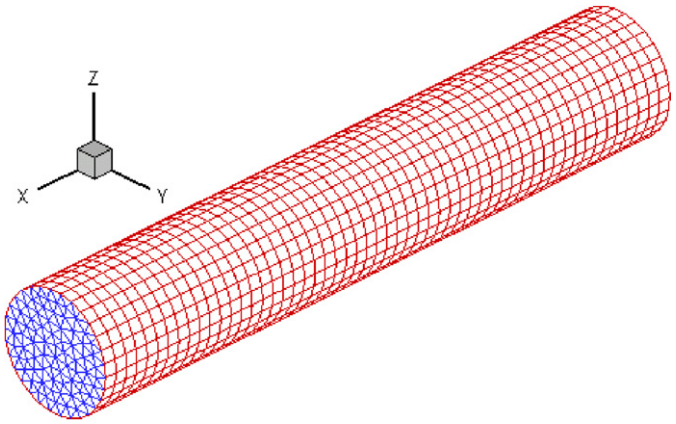

Fig. 2. Computational grid with 1736 nodes used for the circular cylinder configuration ($L = 405.5$ mm, $R = 38$ mm).

at each instant, and f_{ex} denotes the excitation frequency of the forced displacement of the membrane. These conditions correspond to a non-uniform imposed displacement of the membrane $x_{i,j,k}(t)$ with a random amplitude $\chi_{i,j,k}$ at each time step. The excitation frequencies f_{ex} are prescribed using a time-dependent formulation corresponding to a linear variation over a user-defined bandwidth of interest

$$f_{ex}(t) = f_{low} + (f_{high} - f_{low})\frac{t}{t_{max}}, \tag{7}$$

where f_{low} and f_{high} are the lower and the upper values of the excitation window and $t_{max} = n_{max}\Delta t$ is the total simulation time. The duct was excited at a single axial position ($x/L = 0$), while the response was computed at 13 equally spaced points along the duct in order to be able to identify the mode shapes. The variation of the applied excitation frequency against time was defined as $[f_{low}; f_{high}] = [100\,\text{Hz}; 1\,\text{kHz}]$. The maximum amplitude of the membrane displacement was chosen such that the corresponding pressure perturbation was 0.5% of the unperturbed pressure. The corresponding frequency increment is $(\Delta f)_{ex} = (n_{max}\Delta t)^{-1} = 8.13\,\text{Hz}$, the total number of time instants being $n_{max} = 8196$ and the time step $\Delta t = 1.5 \times 10^{-5}$ s. A 3-D unstructured Favre–Reynolds averaged Navier–Stokes solver, based on a $O(\Delta x^2)$ node centered finite-volume scheme with a $O(\Delta t^2)$ implicit dual time stepping technique [23] was used to implement the deterministic excitation boundary condition. The size of the time step was chosen to have 66 points per period in order to ensure the correct time discretization of the signal at the highest excitation frequency $f_{high} = 1\,\text{kHz}$.

The time history of the axial velocity at $x = 0$ (Fig. 3) exhibits the expected random behavior of the excitation signal whereas the flow response at $x = L/2$ (Fig. 4) clearly shows two vibration modes at two distinct instants ($t_1 \cong 5.5 \times 10^{-2}$ s, $t_2 \cong 1.05 \times 10^{-2}$ s), corresponding approximately to 450 and 800 Hz. Both the pressure and velocity signals were stored at each time step and the spectra at each output point were computed by averaging the Fourier transforms of each output $n_o \in [1, N_o]$

$$\bar{X}_u(f) = \frac{1}{N_o}\sum_{n_o=1}^{N_o}\left[\int_0^T u_{n_o}(t)\mathrm{e}^{-i2\pi ft}\,\mathrm{d}t\right], \tag{8}$$

where u_{n_o} is the instantaneous velocity at output n_o and $\bar{X}_u$ the averaged velocity spectrum over the N_o outputs. A typical velocity spectrum is presented in Fig. 5. The two distinct peaks lead to the identification of the acoustic resonant conditions.

The present methodology was applied to 3 different duct lengths ($L = 231$, 292.5, 405.5 mm) and compared with analytically derived resonance frequencies values $f_n^{exact} = n(a/2L)$ for a closed circular cylinder, where a is the speed of sound and n denotes the mode number. The discrepancies between the computed and the analytical results are below the frequency resolution ($\Delta f = 8.13\,\text{Hz}$) for both first two axial modes except for the shorter booster length $L = 231$ mm ($f^{comp.} = 710\,\text{Hz}$ and $f^{exact} = 742\,\text{Hz}$). The axial mode shapes were

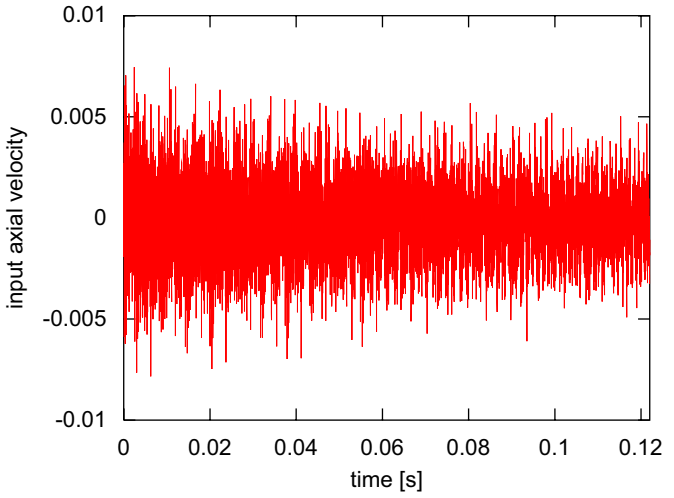

Fig. 3. Time-history of the axial velocity excitation imposed at the inflow ($x/L = 0$).

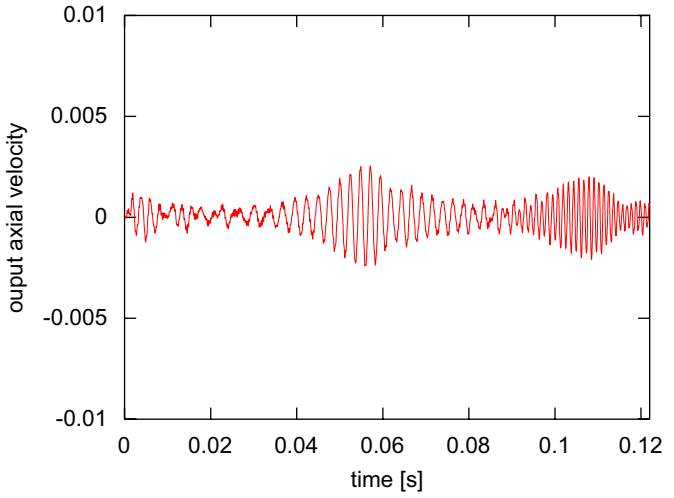

Fig. 4. Time-history of the axial velocity response taken at the middle axis of the duct ($x/L = 0.5$).

determined by considering the peak value of each output spectrum at the two acoustic frequencies. As it can be seen from Fig. 6, the computed non-dimensional pressure mode shape is in good agreement with the exact solution $\Phi^n(x) = \cos(n\pi x/L)$. The wavelength of the first acoustic mode is twice the length of the cylinder and the wavelength of the second acoustic mode is equal to the length of the cylinder. Furthermore, as predicted by theory, an inspection of Figs. 6 and 7 reveals that there is a phase shift of a quarter wavelength between the pressure and velocity mode shapes.

4.1. *Influence of the frequency excitation range*

In addition to the previous results, the velocity spectrum $\bar{X}_u$ was computed for three different excitation cases: (a) [50−999 Hz]; (b) [100−600 Hz]; and (c) [300−900 Hz]. All computations were performed with $\Delta t = 1.5 \times 10^{-5}$ s and $n_{\max} = 8192$. The results are presented in Fig. 8 and the effect of the excitation range on the predicted frequencies is self evident. Case (b) captures the first axial mode only ($f^{1A} = 420$ Hz) since the second mode is outside the range. Case (c), the excitation window of which has been extended compared to case (b)

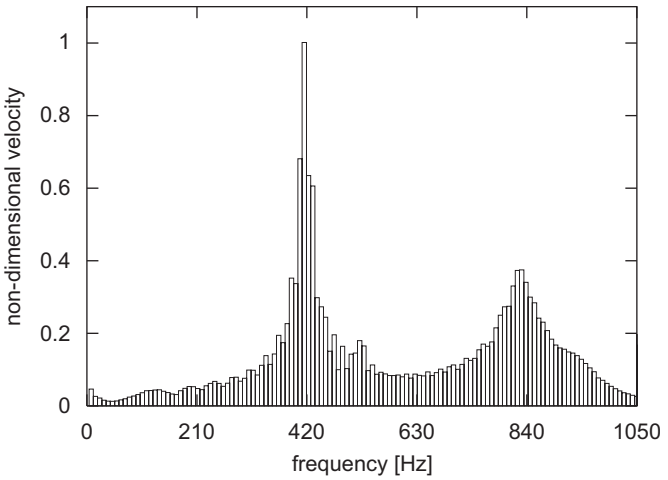

Fig. 5. Velocity spectrum using non-uniform time-dependent random forcing (Eq. (6), (7); the amplitude is dimensionless using the amplitude of the first axial mode; exact resonance frequencies are $f^{1A}_{\text{exact}} = 423\,\text{Hz}$ and $f^{2A}_{\text{exact}} = 846\,\text{Hz}$).

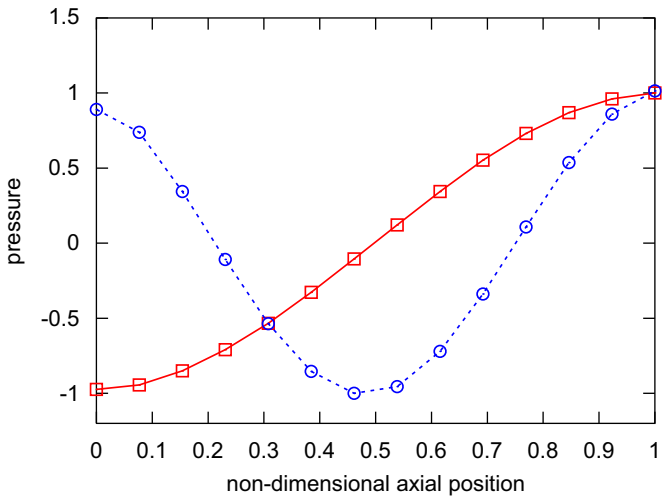

Fig. 6. Predicted pressure mode shapes for the first two fundamental modes—Randomly vibrating (—— 1st axial mode ($f^{1A} = 419\,\text{Hz}$); – – – 2nd axial mode ($f^{2A} = 838\,\text{Hz}$)).

(Fig. 8), is seen to capture both modes ($f^{1A} = 420\,\text{Hz}$ and $f^{2A} = 840\,\text{Hz}$). Case (a), which uses a broad bandwidth, also captures both modes but the peak amplitudes are seen to be different. When the excitation range is below 200 Hz, there is no flow response for case (c) because the excitation window is located apart from significant frequencies (Fig. 8). Otherwise, there is a flow response for cases (a) and (b) for $f_{\text{ex}} < 200\,\text{Hz}$ (Fig. 8). This relatively small but not negligible amplification between cases (a), (b) and case (c) represents approximately 8% of the first mode peak amplitude and may be assimilated to the level of the residual noise introduced by the solver.

4.2. *Effect of the time step*

Two numerical simulations, corresponding to time steps of $\Delta t = 1.5 \times 10^{-5}\,\text{s}$ and $\Delta t = 8 \times 10^{-6}\,\text{s}$, were conducted on a cylinder with a length of $L = 231\,\text{mm}$. The time record lengths were $n_{\max} = 8192$ and 16384, respectively. The corresponding computed pressure spectrum amplitudes are plotted in Fig. 9. Both

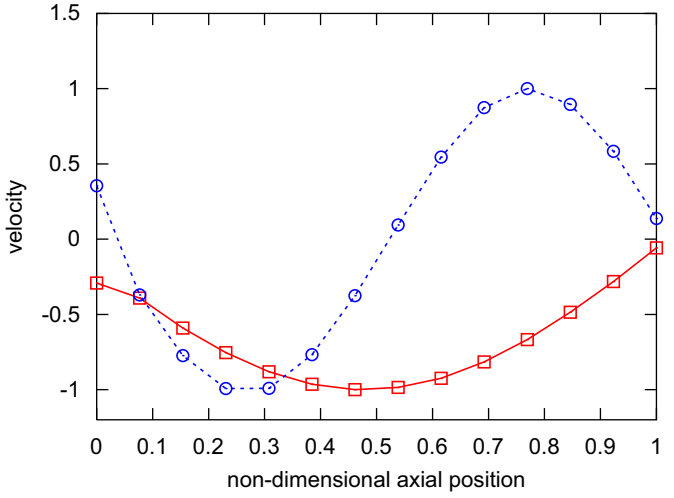

Fig. 7. First two fundamental velocity mode shapes—Randomly vibrating wall (— 1st axial mode ($f^{1A} = 419$ Hz); – – – 2nd axial mode ($f^{2A} = 838$ Hz)); $L = 405.5$ mm.

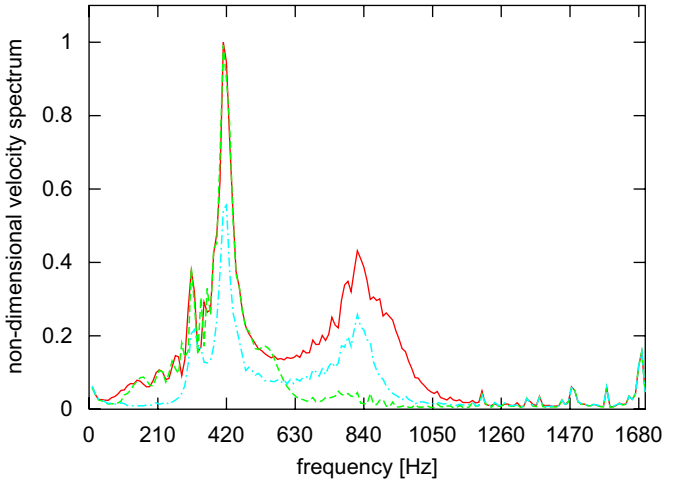

Fig. 8. Influence of the excitation frequency window for the configuration $L = 405.5$ mm (— case (a) [50 Hz; 999 Hz]; – – – case (b) [100 Hz; 600 Hz]; —·— case (c); [300 Hz; 900 Hz]; $f^{1A}_{\text{exact}} = 423$ Hz, $f^{2A}_{\text{exact}} = 846$ Hz).

computations were able to capture the resonant frequency of the first longitudinal mode, the value of which agrees with the analytical solution ($f^{1A}_{\text{exact}} = 742$ Hz). However, it is immediately seen that the shorter time step, with 168 points per period, yields a much clearer spectrum than the longer time step which only has 90 time steps per period. The second axial mode ($f^{2A}_{\text{exact}} = 1485$ Hz) was not captured by the numerical simulations because the excitation frequency window was selected to capture the first mode only.

4.3. *Influence of the excitation mechanism*

Finally, cylinder dimensions of $L = 1$ m and $D = 0.5$ m were selected in order to investigate the influence of membrane behavior on the flow excitation. The discretization of the cylinder geometry resulted in 31 equally spaced circumferential nodes and 49 axial nodes, the total number of grid points being 4998. A time step of

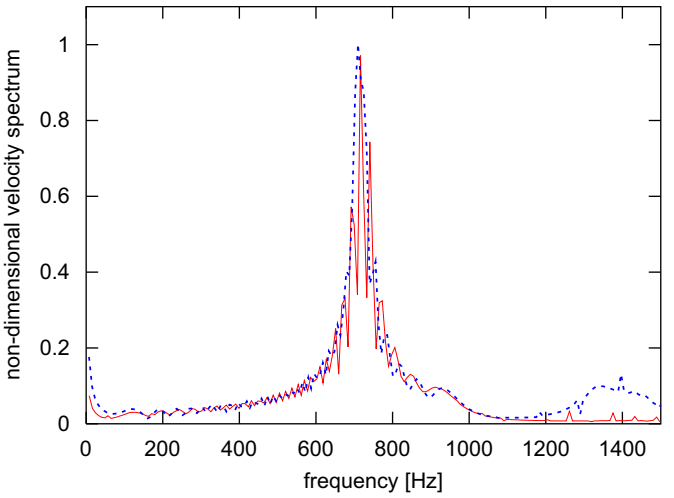

Fig. 9. Effect of the time step for the configuration $L = 231\,\text{mm}$ (—— $\Delta t = 1.5 \times 10^{-5}\,\text{s}$; – – – $\Delta t = 0.8 \times 10^{-5}\,\text{s}$; $f^{1A}_{\text{exact}} = 742\,\text{Hz}$).

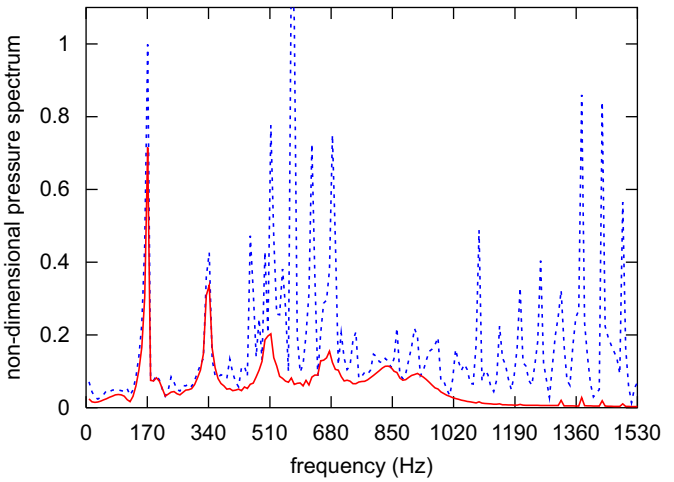

Fig. 10. Comparison of the velocity spectrum amplitude resulting from different random excitation mechanisms (—— deforming piston excitations; – – – solid piston excitations; $L = 1\,\text{m}$, $f^{1A}_{\text{exact}} = 170\,\text{Hz}$, $f^{2A}_{\text{exact}} = 340\,\text{Hz}$, $f^{3A}_{\text{exact}} = 510\,\text{Hz}$).

$\Delta t = 1.5 \times 10^{-5}\,\text{s}$ and an excitation window of [10 Hz; 999 Hz] were used. The maximum amplitude of the vibrating membrane corresponds to a 1% variation of the steady pressure inside the cylinder. Additional numerical parameter are $n_{\max} = 4096$, $T = 6.1 \times 10^{-2}\,\text{s}$ and $\Delta f = 8.13\,\text{Hz}$. Two sets of calculations, corresponding to elastic and rigid membranes respectively, were considered. The rigid membrane calculation was performed by setting the axial displacement of the membrane, denoted by χ in Eq. (6), to a constant value, independent of grid position. The results are plotted in Fig. 10 which clearly shows that the use of an elastic membrane is a much better way of exciting the flow. Although the rigid membrane is able to capture the first two modes, it also introduces spurious oscillations which hinder the identification of the third and fourth modes in Fig. 10. The first three mode shapes obtained from the elastic membrane calculation are plotted in Fig. 11. The time step corresponds to 392 time points per period used to describe the fundamental acoustic mode ($f^{1A} = 1.7\,\text{kHz}$). Although the mode shapes are captured with good accuracy, a small deformation occurs near the membrane at $x = 0$ because the grid points at that location are moving with the mesh to provide the membrane flexibility.

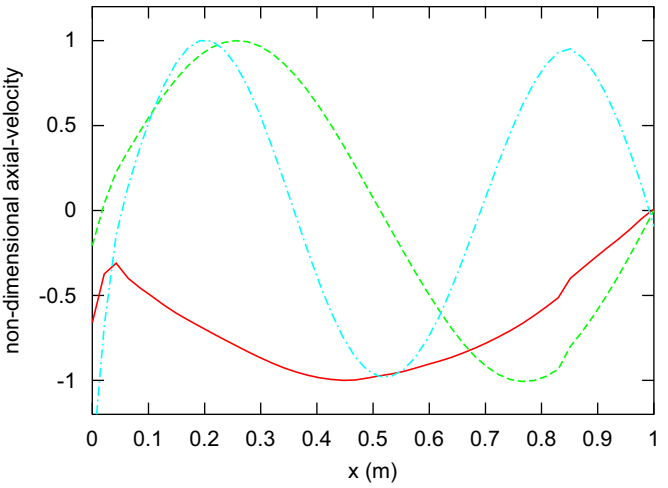

Fig. 11. First three velocity mode shapes in a closed cylinder of length $L = 1$ m resulting from a random deformation of the wall (—— 1st mode ($f^{1A} = 170$ Hz); – – – 2nd mode ($f^{2A} = 340$ Hz); —·— 3rd axial mode at $f^{3A} = 510$ Hz).

5. Test-case 3: acoustic characterization of the Délery B nozzle

Here, the aim is to demonstrate the capability of the method to deal with practical flows. 2-D RANS computations were performed on the Délery B symmetric bump channel with an adjustable second throat [24]. This nozzle has a length of $L = 629$ mm and a height of $H = 100$ mm and the inlet flow velocity is $u_0 = 17\,\mathrm{m\,s^{-1}}$. The minimum sections at the first and second throats are located at $x_{T_1} = 90$ mm and $x_{T_2} = 550$ mm, respectively (Figs. 12 and 13). Steady flow solution, which is used to start the unsteady simulation, was computed using a multi-block structured Favre–Reynolds-averaged Navier–Stokes solver with $O(\Delta x^3)$ upwind-biased van Leer-flux-vector-splitting scheme and Reynolds-stress model [25]. Time accurate simulations are based on an implicit $O(\Delta t^2)$ dual-time-stepping procedure with alternating-direction-implicit sub-iterations [25]. Furthermore, it is assumed that no spectral interactions exist between the deterministic driven unsteadiness and turbulence [27]. Consequently, statistical turbulence closures developed for the Favre-averaged Navier–Stokes equations are used to compute the flow with unsteady boundary conditions.

The computational mesh is based on 201×101 grid points in the streamwise (x) and wall-normal (y) directions, respectively (Fig. 12) and the minimum non-dimensional grid spacing at the wall is $y_w^+ = 0.5$. In this study, the excitation was chosen generated by rigid and elastic vertical displacements of the upper wall corresponding to the convergent-divergent parts of the 2nd throat ($x \in [550\,\mathrm{mm},\ 629\,\mathrm{mm}]$). The computational grid is displaced at each physical time step to follow the deformation of the second throat. The grid velocities necessary for the definition of the numerical fluxes are computed by solving a Laplace equation [26]. An array of 14×7 (x-wise$\times y$-wise) "pressure sensors" was used to compute the FRF matrix (Fig. 13). The time step was set to $\Delta t = 7 \times 10^{-6}$ s and the total computational time $T = 0.11$ s corresponds to a frequency resolution $\Delta f = 8$ Hz.

A preliminary study was conducted on the unsteady flow response resulting from two different deformations of the 2nd throat. Fig. 14 presents a comparison of the pressure amplitude spectra at probe $x = 350$ mm and $y = 30$ mm resulting from random displacements of the 2nd throat and from sine sweep oscillations. As expected, both approaches give the same acoustic resonance frequencies, but it appears that the white noise excitation yields noisier pressure spectra than a sine sweep excitation (Fig. 14). Therefore, further studies will be performed by imposing a sine oscillation to the 2nd throat (Fig. 15).

It can be seen from Fig. 16 that the pressure time history of the flow response, picked up at the reference probe, exhibits a high response level at selected frequencies. This is confirmed by the amplitude and phase plots of the pressure spectrum (Fig. 17). It must be noted that these spectra, which are computed without the use of FRF windowing or sample averaging procedures, are completely free from spurious noise. As pointed

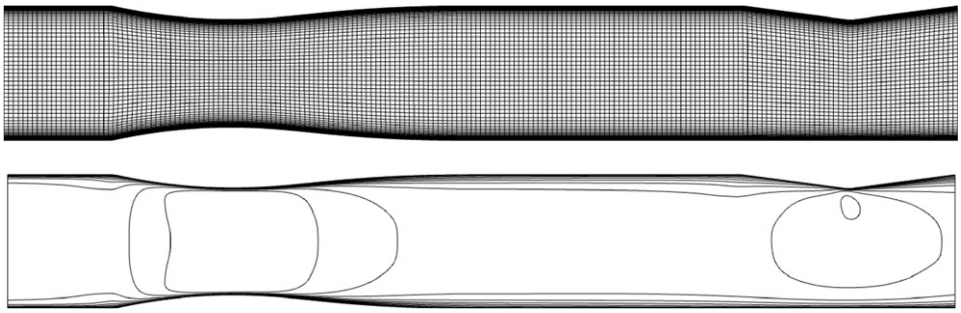

Fig. 12. Computational grid for the Délery B nozzle ($Ni \times Nj = 201 \times 101$) and steady-state Mach number for an inlet flow velocity $u_0 = 17\,\mathrm{m\,s^{-1}}$.

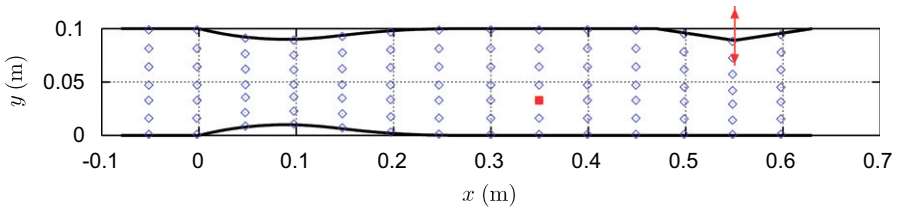

Fig. 13. Positions of the "pressure sensors" (square symbol indicates the location of the reference sensor: $x = 350\,\mathrm{mm}$, $y = 30\,\mathrm{mm}$ used to analyze the pressure spectra).

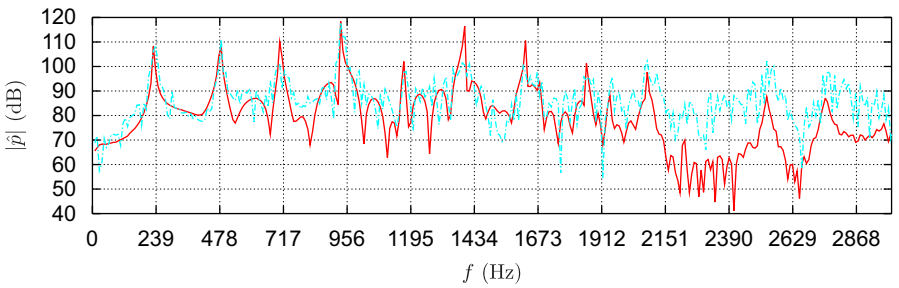

Fig. 14. Influence of the unsteady flow response due to random excitation and sine sweep excitation on the pressure spectrum amplitude (— sine sweep excitation; -·- random excitation).

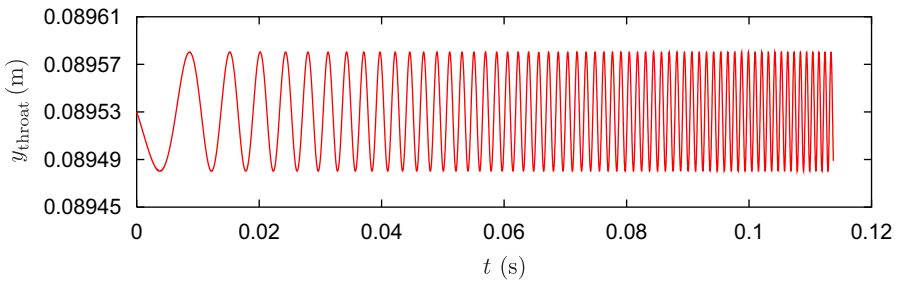

Fig. 15. Vertical displacement of the 2nd throat due to sine-sweep excitations for the 100 Hz–3 kHz range.

out by the reviewers, this is probably due to the fact that the RANS solver acts as a low-pass filter. The resonance conditions, which are characterized by peaks in the pressure spectrum amplitude, are clearly visible up to 3 kHz (Fig. 17). As expected, the first resonance frequency ($f_1 = 237\,\mathrm{Hz}$) matches closely the

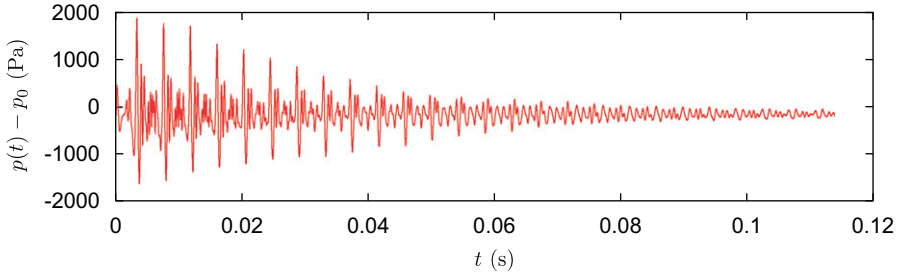

Fig. 16. Time history of the pressure fluctuation extracted at point $x = 350\,\text{mm}$ and $y = 30\,\text{mm}$.

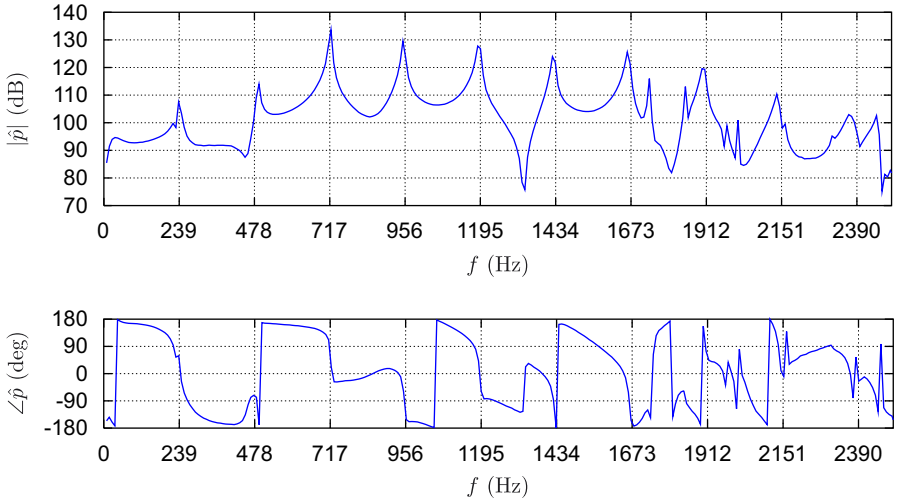

Fig. 17. Frequency response of the pressure signal at point $x = 350\,\text{mm}$ and $y = 30\,\text{mm}$.

analytically-computed axial acoustic modes assuming zero mean-flow ($f^{1A}_{\text{exact}} = 239\,\text{Hz}$). The Strouhal number, based on the bump length χ is $Sr = f^{1A}\chi/u_0 = 2.8$ for the first acoustic mode. It is interesting to note that the pressure spectrum shows, in the 1700–2100 Hz frequency range, two peaks whose frequencies ($f_8 = 1731\,\text{kHz}$ and $f_9 = 1845\,\text{Hz}$) do not correspond to a multiple of the fundamental axial mode ($f_8/f_1 = 7.3$ and $f_9/f_1 = 7.78$). Additional information is given by Fig. (18) which presents the acoustic mode shapes for the first 10 resonance frequencies. It is clear that the present methodology is able to capture a pure transverse mode, mode 8 in Fig. 18. The frequency of this mode is $f_8 = 1731\,\text{Hz}$ which is close to the first pure transverse acoustic mode based on the nozzle height ($f^{1T}_{\text{exact}} = 1700\,\text{Hz}$). Furthermore, a coupled axial-transverse mode, mode 9 in Fig. 18, is predicted at $f_9 = 1845\,\text{Hz}$. Other mode shapes ($n = 1, \ldots, 7, 10, 13, 14$) can be assimilated to pure longitudinal modes because their resonance frequencies are close to a multiple of the first axial mode.

6. Concluding remarks

• The purpose of this study was to assess if a time-domain CFD code could be used to predict acoustic resonances. The methodology is based on a combination of the well-known MIMO vibration-testing procedure and acoustic excitation using loudspeakers. The shakers are replaced by elastically deforming vibrating membranes and the fluid/structure system is characterized by using a time-domain CFD code. The simulated acoustic field is monitored at a sufficient number of points to define the mode shapes. It was found both white noise and sine sweep excitations are able to predict the correct resonance frequencies and the corresponding pressure mode shapes.

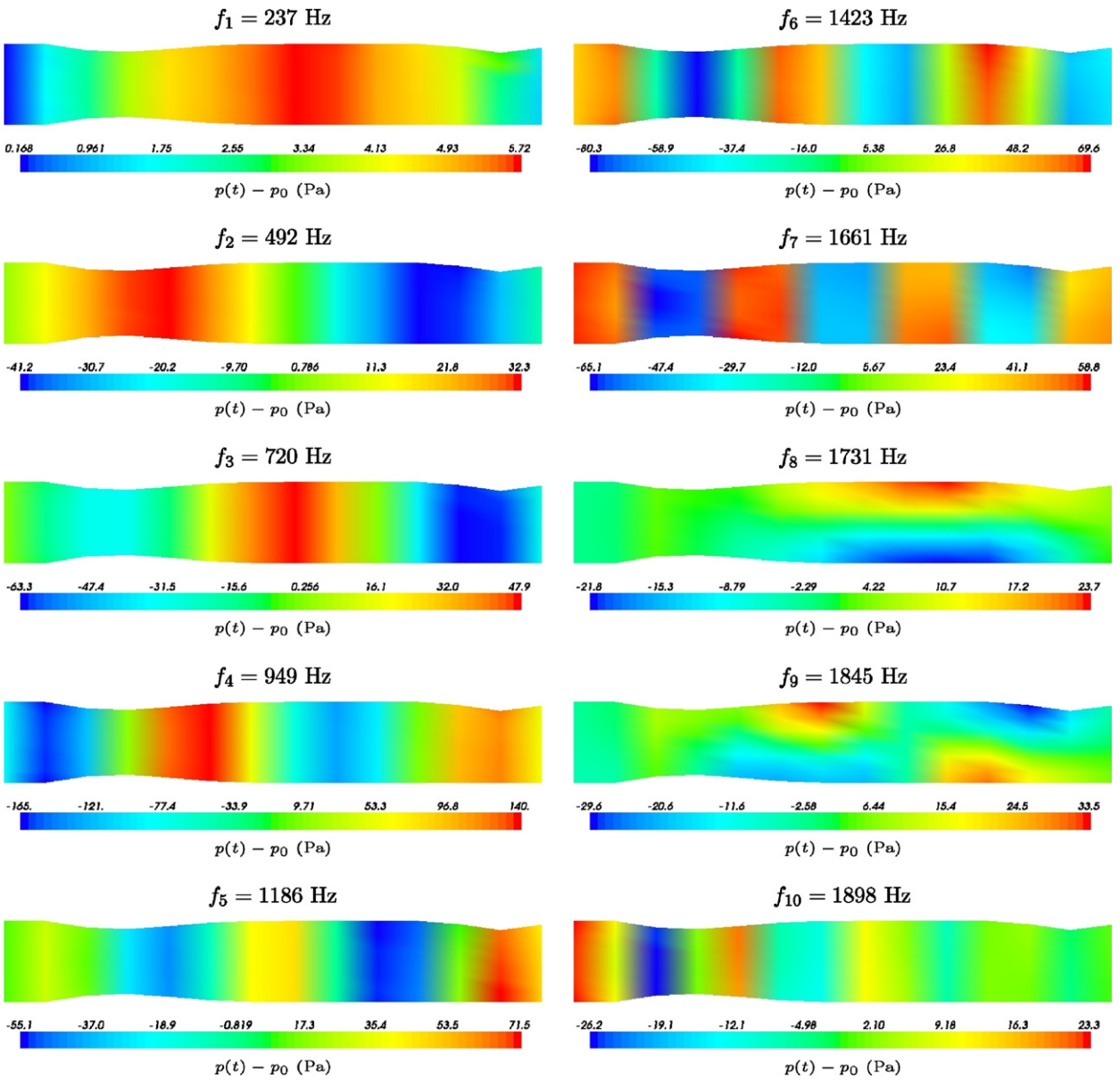

Fig. 18. Acoustic modes of the Délery nozzle for an inlet flow velocity $u_0 = 17\,\mathrm{m\,s^{-1}}$ ($\Delta t = 6.94 \times 10^{-6}\,\mathrm{s}$, $T = 0.113\,\mathrm{s}$, $\Delta f = 8\,\mathrm{Hz}$, $\Delta_h = 0.1\,\mathrm{mm}$).

• The results indicate that it is possible to perform the acoustic mode identification with good accuracy up to about 3 kHz. In the case of the Délery nozzle, the sine sweep excitation mechanism allows the identification of a large number of acoustic modes. It must be noted that this global aeroacoustic characterization requires only one unsteady RANS computation over a total simulation time corresponding to 30 periods of the fundamental acoustic mode. A second advantage of the method is that it takes, by virtue of using a full CFD model, into account mean flow velocities, turbulence effects and temperature variations. Therefore, it is applicable to complex geometries and flow conditions typical of aero-engine applications. Nonetheless, further work is needed to study the potential effects of numerical dissipation on pressure spectrum amplitudes.

References

[1] R.E. Brahimi, R.E. Brahimi, A. Ghafourian, Mode identification of high-amplitude pressure waves in liquid rocket engines, *Journal of Sound and Vibration* 229 (2000) 973–991.

[2] Z.-S. Liu, C. Huang, W.-M. Qian, Z.G. Liu, L.-Y. Jiang, I. Campbell, I. Yimer, Self-excited combustion oscillations of a burner: cause and remedy, *10th International Congress on Sound and Vibration*, Stockholm [S], July 7–10, 2003.

[3] K. Hourigan, M.C. Welsh, M.C. Thompson, A.N. Stokes, Aerodynamic sources of acoustic resonance in a duct with baffles, *Journal of Fluids and Structures* 4 (1990) 345–370.

[4] M.C. Welsh, K. Hourigan, L.W. Welsh, R.J. Downie, M.C. Thompson, A.N. Stokes, Acoustics and experimental methods: the influence of sound on flow and heat transfer, *Experimental Thermal and Fluid Science* 3 (1990) 138–152.

[5] J.C. French, Three-dimensional combustion stability modeling for solid rocket motors, AIAA Paper 98–3702, 1998.

[6] S. Ziada, A. Oengoren, A. Vogel, Acoustics resonance in the inlet scroll of a turbo-compressor, *Journal of Fluids and Structures* 16 (2002) 361–373.

[7] S. Pirozzoli, F. Grasso, Direct numerical simulation of impinging shock wave/turbulent boundary layer interaction at $M = 2.25$, *Physics of Fluids* 18 (2006).

[8] C.Y. Loh, K.B.M.Q. Zaman, Numerical investigation of ''transonic resonance'' with a convergent-divergent Nozzle, NASA/TM 2002-211324, 2002.

[9] M. Debiasi, M. Samimy, Logic-based active control of subsonic cavity flow resonance, *AIAA Journal* 42 (2004) 1901–1909.

[10] L.-E. Eriksson, L. Andersson, K. Lindblad, N. Andersson, Development of a cooled radial flameholder for the F404/RM12 afterburner: part III, afterburner rumble prediction and suppression, ISABE Paper 2002–1060, 2003.

[11] J. Anthoine, P. Planquart, D. Olivari, Cold flow investigation of the flow acoustic coupling in solid propellant boosters, AIAA Paper 98–0475, 1998.

[12] J. Anthoine, D. Olivari, S. Hulshoff, M. Van Rooij, Qualitative model of vortex induced oscillations in a model of solid propellant boosters, AIAA Paper 98–2270, 1998.

[13] J. Anthoine, J.-M. Buchlin, J.-F Guéry, Experimental and numerical investigations of nozzle geometry effect of the instabilities in solid propellant boosters, AIAA Paper 2000–3560, 2000.

[14] J. Anthoine, J.-M. Buchlin, A. Hirschberh, Theoretical modelling of the effect of the nozzle cavity volume on the resonance level in large solid rocket motors, AIAA Paper 98–2102, 1998.

[15] A.K. Stubos, C. Benocci, E. Palli, G.K. Stoubos, D. Olivari, Aerodynamically generated acoustic resonance in a pipe with annular flow restrictors, *Journal of Fluids and Structures* 13 (1999) 755–778.

[16] H. Osman, M. Johnson, C. Fuller, P. Marcotte, Interior noise reduction of composite cylinders using distributed vibration absorbers, AIAA Paper 2001–2230, 2001.

[17] K.R. Holland, P.O.A.L. Davies, The measurement of sound power flux in flow ducts, *Journal of Sound and Vibration* 230 (2000) 915–932.

[18] K.R. Holland, P.O.A.L. Davies, D.C. van der Walt, Sound power flux measurements in strongly excited ducts with flows, *Journal of Acoustical Society of America* 112 (2002) 2863–2871.

[19] C. Armitage, S. Cant, A. Dowling, T. Hunes, Linearised theory for 1pp combustion dynamics, ASME Paper GT 2003–38670, 2003.

[20] R.B. Bravo, S. Ziada, M. Dokainish, Aeroacoustic response of an annular duct with coaxial closed side branches, AIAA Paper 2005–3019, 2005.

[21] G. Avalon, Th. Josset, Cold gas experiments applied to the understanding of aeroacoustic phenomena inside solid propellant boosters, AIAA Paper 2006–5111, 2006.

[22] J.S. Bendat, A.G. Piersol, *Random Data*, second Ed., Wiley, New York, 1986.

[23] A.I. Sayma, M. Vahdati, L. Sbardella, M. Imregun, Modelling of 3D viscous compressible turbomachinery flows using unstructured hybrids grids, *AIAA Journal* 38 (2000) 945–954.

[24] J.M. Délery, Experimental investigation of turbulence properties in transonic shock/boundary-layer interactions, *AIAA Journal* 21 (1983) 180–185.

[25] J.-C. Chassaing, G.A. Gerolymos, I. Vallet, Efficient and robust computation of 3-D compressible flows with Reynolds-Stress closure, *AIAA Journal* 41 (2003) 763–773.

[26] J.-C. Chassaing, G.A. Gerolymos, I. Vallet, Reynolds-stress model dual-time-stepping computation of unsteady 3-D flows, *AIAA Journal* 41 (2003) 1882–1894.

[27] J.-C. Chassaing, G.A. Gerolymos, I. Vallet, Turbulence structure modification from low-frequency shock-wave micro-oscillations, AIAA Paper 4116, 2007.